Article

Flexible Bending Sensors Fabricated with Interdigitated Electrode Structures Cross-Linked by Transition Metal Doped ZnO Nanorods

Waqar Muhammad and Sam-Dong Kim *

Division of Electronics and Electrical Engineering, Dongguk University, Seoul 100-715, Republic of Korea; waqar6414@dgu.ac.kr
* Correspondence: samdong@dongguk.edu; Tel.: +82-2-2260-3800

Abstract: Bending strain sensors based on one-dimensional ZnO nanorod (NR) arrays cross-linked with interdigitated electrodes were fabricated on polyethylene terephthalate (PET) substrates. ZnO NRs were grown using the hydrothermal method through the dopings with different transition metals, such as Co, Ni, or Co-plus-Ni, on PET substrates, and their microstructural morphology and crystalline properties were examined by a variety of surface analysis methods. Ultraviolet photoresponse and normalized resistance change were measured according to the bending strains to concave and convex directions, and the highest gauge factors of 175 and 83 were achieved in the convex and concave directions, respectively, at a bending strain of 1.75%, when Co-plus-Ni was doped to the NRs.

Keywords: ZnO nanorods; bending sensors; flexible; transition metal doping; interdigitated electrodes

1. Introduction

Flexible and wearable electronics have evolved rapidly over the past decades, and a variety of application systems, including sensors, electronic skin, batteries, super-capacitors, solar cells, heaters, and stretchable transparent electrodes, have been intensively developed by earlier research [1]. Flexible sensors can be one of the key component materials for future smart sensing systems such as electronic components, smart robotics, electrical stimulation for the human body, medical instruments, environmental monitoring, and protective space travel [2]. To provide more improved reliability and sensitivity to these sensors, intensive research effort has also focused on the use of nanostructures synthesized in many ways and using different materials. The chemical or physical functions of many nanostructures could be efficiently utilized for their sensing application to ensure higher sensitivity and selectivity [3,4]. Another important feature is their potential to vary the dimension and shape of these nanostructures; this would allow us to control the surface properties (variable ratio between surface and volume) of nanomaterials, thereby creating challenging characteristics when responding to strain, temperature, gas, plasmon resonance, etc. [5,6]

Numerous types of one- or two-dimensional nanomaterials have been highlighted for flexible sensor applications [7–11]. Among them, zinc oxide (ZnO) has been investigated as a promising nanostructured material for the combined properties of semiconducting with piezoelectric, as well as for its stable and highly safe material properties [7,11,12]. Many synthesis techniques for ZnO nanorods (NRs) have been reported thus far; however, they can be categorized into two groups of vapor phase deposition and solution-based growth. Pulsed laser deposition, metal organic vapor deposition, chemical vapor deposition, and physical vapor deposition are the cases of vapor phase deposition; however, solution-based synthesis method is, in general, more advantageous in terms of its low process temperature, no requirement for sophisticated equipment, and low manufacturing cost [12].

The hydrothermal method belongs to this growth technique and is specifically performed based on a water solution.

ZnO nanostructures were investigated by many research groups for the construction of high-sensitivity ultraviolet (UV) photodetection operating in visible-blind range [11,13] owing to their unique material properties, making them suitable for UV photonic applications (direct bandgap of ~3.37 eV, exciton binding energy of 60 meV). They have also been examined as a potential material for various application systems such as gas sensors, bio-sensors, nanogenerators, and optoelectronic devices (laser diodes, light emitting diodes, and solar cells) [12,14–16]. One-dimensional ZnO nanostructures could change their electrical conductance under bendings with axial or torsional directions; for this, a variety of ZnO based nano-systems were demonstrated in tactile strain sensing applications using flexible substrates and many different sensing architectures, such as the hybrid structure of ZnO nanostructures with graphene, vertically grown ZnO nanocrystals on polyethylene terephthalate (PET), and fine ZnO wires [7,17–20]. The hydrothermal growth method for ZnO NR array can be performed at significantly low temperatures, making it suitable for growth on plastic substrates such as PET (thermally deformed at higher than 150 °C), as used in this study. Furthermore, we can efficiently dope the NRs with transition metals (TMs) in growth solutions [7,21,22]. The oxygen vacancies, mobility, and conductivity of ZnO NRs were found to be greatly dependent on the doping of TMs such as Co, Ni, Mn, Cu, and Fe. ZnO grown by a hydrothermal scheme is oxygen-deficient in nature and considered a good host for TM dopants, enhancing the electrical properties by modulating mobility, intrinsic defects, and different bandgap and optical/magnetic properties.

We present, in this article, the fabrication method and sensing characteristics of bending sensor devices with a unique design based on ZnO nanocrystals hydrothermally grown on micro-fabricated interdigitated electrode (IDE) structures. The electric current of the fabricated sensor devices is transported between the IDEs through a number of one-dimensional conductive materials, and the change in current is characterized on the bending strain in either the concave or convex direction. We investigated the effects of doping the ZnO NRs with specific TMs (Co-, Ni-, or Co and Ni-co-doped) on the crystalline quality of ZnO crystals and sensing performance of devices. For this, we utilized various material characterization methods for crystal growth modes, chemical/optical properties, and structural properties of the NRs. To substantiate the influence of examined TM-doped material properties on the sensing performance, we evaluated the performance parameters of fabricated devices with IDE patterns.

2. Materials and Methods

The sensor device fabricated in this study is shown in the top-right of Figure 1 with a magnified view for the IDE structure (in the center) formed on PET substrate. Five fingers from the IDE structure form a zipper-like structure, alternating each other to provide the conduction channels by cross-linking ZnO NR arrays, as shown in the top-left and bottom-left of Figure 1. As described in the center and bottom-right micrographs, each dimension of the length, width, and gap spacing of the fingers was defined by 300, 20, and 4 μm, respectively. The fabrication process for the bending sensors was performed in the following sequence. We first cleaned PET substrates (0.35 mm thickness, 92% optical transmission) using acetone and isopropyl alcohol for 10 min each, before rinsing in deionized water and sonicating them to remove the contamination and particles on the surface. After cleaning the surface, we carried out N_2 purging and baking using a hot plate for 60 °C for 1 min. To increase the hydrophilicity of the PET surface by generating hydroxyls and enhance the surface adhesion for the subsequent electrode metals [7], O_2 plasma treatment (PT) was performed in a reactive ion etching system at a pressure of 50 mTorr with an O_2 flow rate of 100 sccm (RF power of 100 W) for 5 min. From this, we increased hydrophilicity on PET substrates (reduced water contact angle of ~75.1° to ~10.9°) after PT. For this, an optical goniometer (model No. 250-U4) using the sessile drop method was used in a tensiometer. We deposited Ti/Au metals (30/80 nm) in an electron-beam evaporator and fabricated the

IDE patterns, as shown in Figure 2a, using photolithography (AZ 5214E photoresist) and the subsequent metal lift-off.
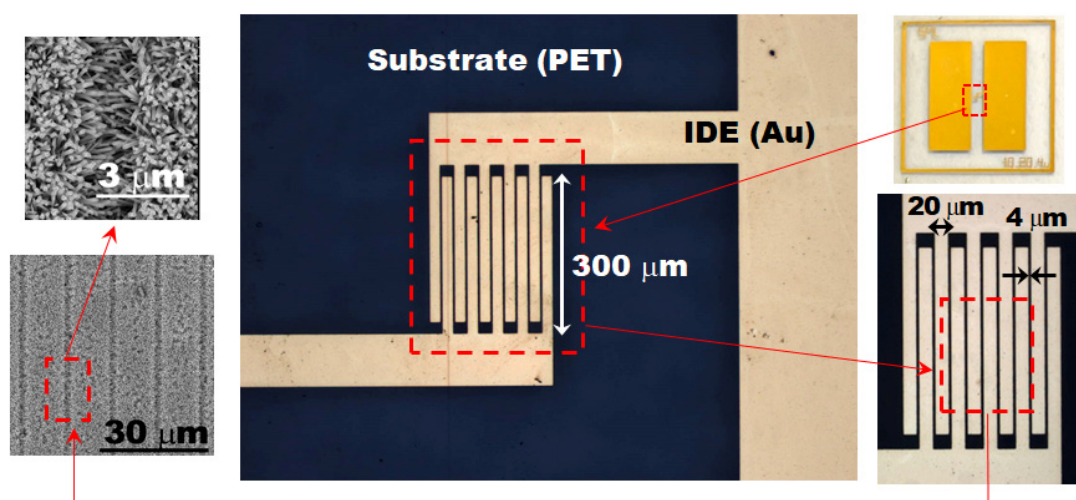

Figure 1. (**top-right**) Plane-view of the fabricated sensor on PET substrate with (**center**) a magnified view of the device. (**bottom-right**) Blown-up view for the IDE region highlighted in the central micrograph. (**bottom-left**) NR array grown atop the IDE structure and (**top-left**) magnified view of the NR array. Reprinted with permission from Ref. [23].
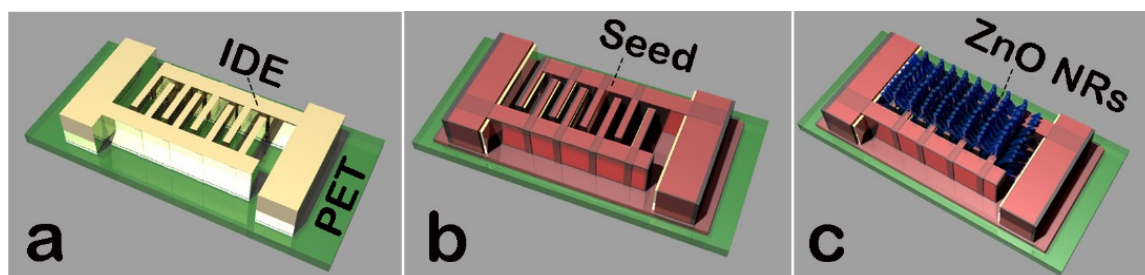

Figure 2. Schematics of process sequence for the sensor device fabrication. After (**a**) IDE metal patterns are formed, (**b**) SL is grown on the active layer. (**c**) NR arrays are grown between the IDE structures.

The active area for the seed layer (SL) to be selectively grown was first defined on the PET substrates (GP-PET-4OP, thickness 0.35 mm, optical transmission 92%) in a photolithography system of MA6 Mask Aligner (Karl Suss, Garching, Germany). All the chemicals (purity > 99%) used in this experiment were purchased from Sigma-Aldrich Korea (Seoul, Republic of Korea). An aqueous colloidal solution of 20 mM zinc acetate dehydrate [$Zn(CH_3COO)_2 \cdot 2H_2O$] in 30 mL 1-propanol, well-stirred by sonication for 30 min, was prepared for the growth of SL, which plays a key role in the nucleation center and has a strong impact on the crystalline quality of ZnO NRs. The SL was then grown by spin-coating the SL solution onto the IDE patterned substrates at 3000 rpm for 30 s, followed by annealing at 98 °C for 1 min, as shown in Figure 2b. This spin-coating was repeated 15 times to achieve a desired SL thickness of ~20 nm (measured by cross-sectional transmission electron microscopy), followed by post-annealing at 150 °C for 1 h to vaporize the remaining organic contaminants and moisture residuals. To grow undoped ZnO NRs (CS: control sample), the samples were immersed in a standard growth solution (an equimolar 25 mM aqueous solution of zinc nitrate hexahydrate [$Zn(NO_3)_2 \cdot 6H_2O$, 99%] and hexamethylenetetramine [HMTA, $C_6H_{12}N_4$, 99.5%]) at 90 °C for 7 hr. To introduce dopants of Co, Ni, and Ni-plus-Co, we prepared the growth solutions by adding 2% cobalt (II) nitrate hexahydrate [$Co(NO_3)_2 \cdot 6H_2O$], 2% nickel (II) nitrate hexahydrate [$Ni(NO_3)_2 \cdot 6H_2O$], and

2% each of cobalt (II) nitrate hexahydrate and nickel (II) nitrate hexahydrate, respectively, into the separate standard growth solutions. A schematic illustration for the grown NR array cross-linked between the IDE structures is shown in Figure 2c. Final cleaning was performed with acetone, isopropyl alcohol, and deionized water in sequence.

Field emission scanning electron microscopy (FE-SEM, Hitachi 4800S, Tokyo, Japan) operating at 15 kV was used to examine the growth morphologies of the NRs synthesized under different doping conditions. X-ray diffraction (XRD) of 2θ patterns from the NRs was recorded using a Dmax-2500 Rigaku (Austin, TX, USA) at Cu K_α 0.154 nm. We examined the stoichiometric information for the chemical bonding of NRs in each doping case using an X-ray photoelectron spectroscopy (XPS, Thermo-fisher scientific, NEXSA, Waltham, MA, USA) spectrometer. Room-temperature photoluminescence (PL) was performed using an RPM 2000 Accent (Bend, OR, USA) to investigate the optical properties of NR crystallites. Near-band edge emission (NBE) and intra-sub-band emissions caused by shallow or deep level defects of ZnO crystals were characterized by using a 325 nm illumination of He-Cd laser (15 points/s scan rate).

Photoresponse characteristics of the sensor devices were investigated using an input monochromatic light filtered from the light source of a broad band Xenon lamp (200–1100 nm, 300 W). A filtered light beam of 370 nm wavelength was passed through a frequency chopper wheel adjusted at 30 Hz with a lock-in amplifier and illuminated on the sample. The active area of the patterned IDE structure was then illuminated by the monochromatic light, and the devices were probed in a probe station connected with a source meter unit. Ethylene tetrafluoroethylene (TeflonTM ETFE) wires were attached to the pad areas of the fabricated devices using the nickel tape for further electrical characterizations under bending stress. Three-dimensionally printed bending molds for different bending directions and radii (10 and 5 mm) were used to sustain the bent shapes of the sensor elements during the I–V measurement process. Bending axis was aligned parallel to the direction of IDE fingers to provide the longitudinal (either tensile or compressive) strain mode applying to each ZnO NR.

3. Results and Discussion

Every NR crystal was grown in the form of a well-shaped hexagonal column of typical wurtzite crystal structure with a flat surface at the top, but the TM (Co, Ni, Co-plus-Ni) dopings exhibited significant influence on the growth morphology of ZnO NR crystallites, as shown in Figure 3. One notes that the average diameter (D) of the NR crystallites was greatly increased from 75 to 109–119 nm when doped with TMs, whereas almost the same length (L) of ~1 μm was measured from the cross-sectional SEM (Figure 3e,f). This accelerated lateral growth of ZnO NRs induced by TM doping can be associated with the suppressed heterogeneous nucleation with a concentration reduction of OH⁻ ions in the solution [24,25]. This nucleation model proposes that the nucleation of ZnO crystals becomes more difficult due to the increased activation energy barrier of heterogeneous nucleation when the external metal dopants are introduced; therefore, the low density of nuclei promotes their lateral growth instead and results in larger diameters of the doped ZnO NRs. Table 1 shows a summary of the measured atomic percentages for zinc and carbon, as well as each TM dopant introduced in the crystals. The degree of stoichiometry O*/(Zn+dopants) is also shown in the table, where O* represents the stoichiometric oxygen component in the host ZnO matrix extracted from Gaussian deconvolution analysis for O1s photoemission peaks [7].

TM dopings also greatly influence the optical properties of NR crystallites, as revealed by the room-temperature PL spectra of Figure 4a. ZnO nano-crystallites grown by solution method at low temperatures, in general, include a variety of extrinsic and/or intrinsic defects. There are many theories and hypotheses about the exact energy locations of these defects and the causes of their creation, and it is true that there are still controversial claims regarding the nature of the defects depending on the differences in growth methods or post-processing treatments [26,27]. Nevertheless, a prominent broadband emission in a

visible range of 400–760 nm is known to be attributed to deep level emissions (DLEs) caused by various types of intrinsic defects in the ZnO crystals. This visible emission is known to be characterized by three distinctive DLE patterns centered at ~550 nm (green emission at ~2.25 eV), 580 nm (yellow emission at ~2.14 eV), and 640 nm (red emission at ~1.94 eV) [7]. All these emissions are associated with different deep level locations and origins, such as oxygen vacancies, oxygen interstitials, zinc vacancies, zinc interstitials, vacancy complexes, hydrocarbons originating from the organic constituents present in the growth solution, and hydroxyl groups formed in aqueous solution [28–30].
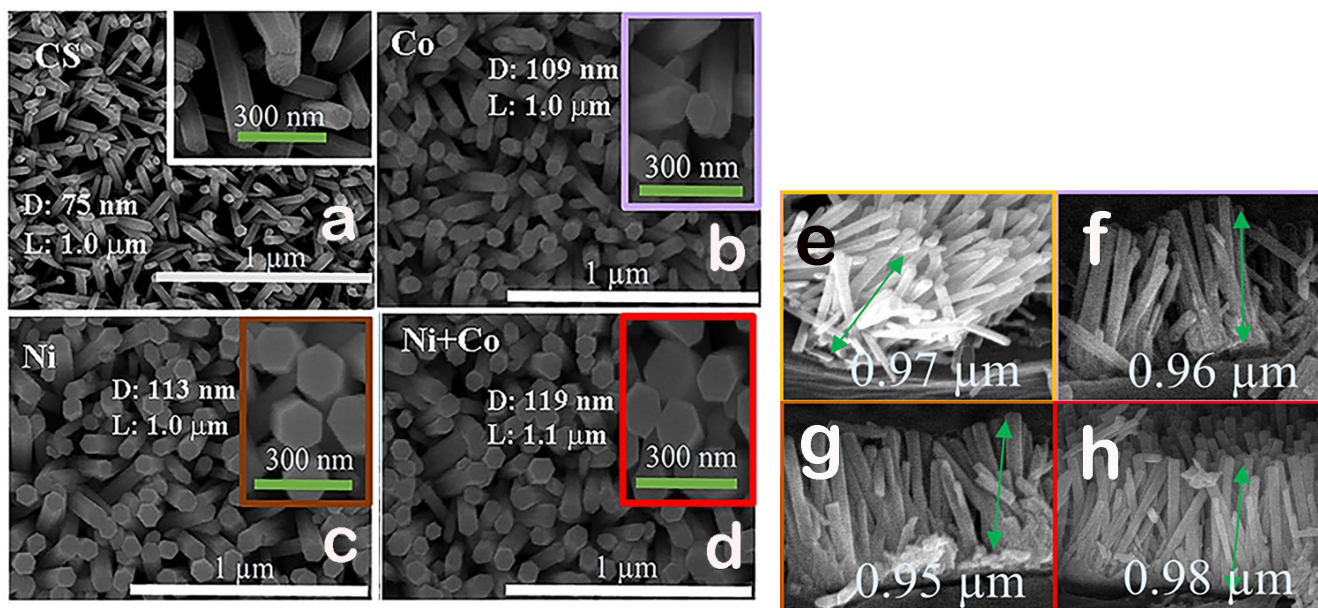

Figure 3. SEM top views of (**a**) undoped, (**b**) Co-doped, and (**c**) Ni-doped, (**d**) Co-plus-Ni-doped ZnO NRs grown on PET substrates. Magnified views for the NRs for each micrograph are shown in the insets. Cross-sectional SEM views of as-grown ZnO NRs for each case of (**a**–**d**) are also shown in (**e**–**h**).

Table 1. Atomic percentage of Co, Ni, Zn, C, and O*/(Zn+dopants) for the NR crystals estimated by XPS analysis. O* is the stoichometric oxygen entity extracted from deconvolution analysis O1s' photoemission peak.

Sample	Co at.%	Ni at.%	Zn at.%	O*/(Zn + Dopants)	C at.%
Undoped	0.00	0.00	37.73	0.55	7.40
Co-doped	0.55	0.00	38.52	0.69	4.19
Ni-doped	0.00	0.59	38.29	0.79	4.24
Co + Ni-doped	0.49	0.37	39.23	0.83	2.86

As shown in Figure 4a, visible emission intensity associated with these deep-level defects was highly suppressed by TM dopings, to less than ~1/2 of the emission from undoped NRs when doped by Co-plus-Ni. On the other hand, UV near-band emission (NBE), which is due to the excitonic band-to-band recombination in ZnO [7], was significantly enhanced by the TM dopings, as shown in the PL spectra. This enhancement by TM dopings, ~5 times higher than that of CS in peak intensity when doped by Co-plus-Ni, suggests that photoluminescence emission was accelerated through the near band-to-band recombination rather than through the deep-level recombinations routed by various intra-subband transitions; that is, it suggests that the crystalline quality of ZnO crystals was effectively recovered by TM doping.
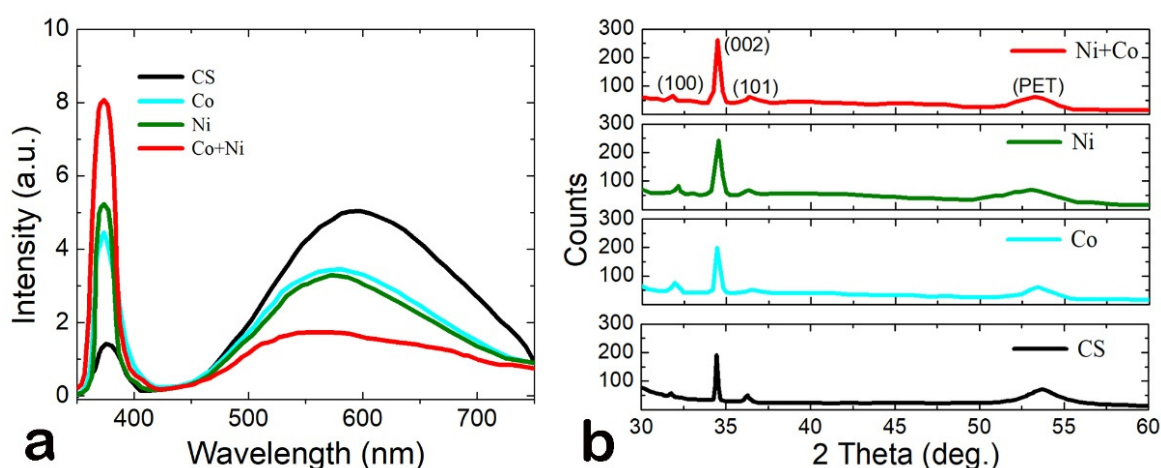
Figure 4. (**a**) Room-temperature PL spectra and (**b**) 2θ scan XRD spectra of ZnO NRs grown by various doping conditions.

The XRD spectra shown in Figure 4b also shows the change in ZnO crystalline quality according to the TM doping. A total of 2θ XRD scans were performed on the NR crystals (2θ = 20–65°) using a 0.02 ° step width and at every step time of 0.2 s to investigate the crystal information and the preferred orientation. All the significant peaks matching with the 2θ positions in standard indexes for crystalline ZnO data (JCPDS files, 36-1451 card numbers) are denoted in Figure 4b. Hydrothermally grown ZnO NR crystals of a hexagonal wurtzite structure have a preferred growth direction to c-axis or [002] in general; therefore, the highest peak is obtained from (002) reflection at 2θ = 34.5 ± 0.02°, which represents that the growth directions of ZnO crystals are in good alignment with the c-axis normal to the substrate direction. To assess the c-axis alignment of NR crystals, the degree of (002) preferred orientation F(002) was calculated using the relationship expressed in Equation (1) [31].
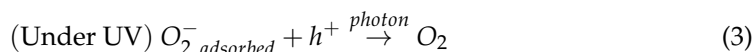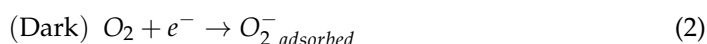
$$F(002) = \frac{P(002) - P_o(002)}{1 - P_o(002)} \tag{1}$$

P(002) and $P_o(002)$, in this equation, are defined by $I(002)/\Sigma I(hkl)$ and $I_o(002)/\Sigma(I_o(hkl)$, respectively, where I(002) is the measured peak intensity from (002) plane, $I_o(002)$ is the reference peak intensity of (002) plane (given by JCPDS card No. 36-1451), ΣI(hkl) is the summation of the intensities of all measured peaks, and $\Sigma I_o(hkl)$ is the summation of the reference intensities of all measured peaks. In Table 2, the F(002) values extracted from each NR crystal were summarized with other key parameters of (002) peak intensity, (002) peak position, and (002) full width at half maximum (FWHM). TM dopings showed a significant improvement in F(002), indicating the degree of c-axis-aligned growth, which was ~20% higher than the CS in the case of Co-plus-Ni doping. The small shift in (002) position toward a higher 2θ when doped with TMs is most likely due to the potential replacement of Zn^{2+} with either Ni^{2+} or Co^{2+} and insignificant differences in the atomic radii of Ni (0.69 Å) and Co (0.72 Å) with that of Zn (0.74 Å) in the host ZnO matrix, as revealed by our recent Cu doping experimental observation [22]. Enhancements in (002) peak intensity and the greatly reduced FWHM observed with TM dopings are also associated with the increased diameters of ZnO crystals [7] (see Figure 3), as well as an improvement in (002) preferred growth.

Table 2. XRD parameters of ZnO NR crystals grown with different TM dopings.

NR Crystals	2θ of (002) (Degree)	(002) Intensity (Counts)	(002) FWHM (Degree)	Degree of (002) Preferred Orientation
Undoped	34.43	191	0.47	0.22
Co-doped	34.45	199	0.37	0.26
Ni-doped	34.46	241	0.35	0.25
Co + Ni-doped	34.47	262	0.33	0.27

To examine the effects of TM doping on the performance of the fabricated bending sensors and the photoresponse characteristics of ZnO NRs carrying the sensing current between the IDEs, two different bending directions, "convex" and "concave", were applied to the sensor elements, as shown in Figure 5(a-1–a-4). Photoresponse characteristics of the wire-bonded sensor devices, resting in the bending molds, were examined inside the dark box connected to the UV light source. Bending strain ε for each bending radius of 10 and 5 mm was 0.0175 and 0.0350, respectively, according to our definition of $\varepsilon = h/2r$ [32], where h is the thickness of the PET substrate (0.35 mm), and r is the bending radius. Figure 5b–f show the I–V characteristics of the sensor devices measured in a voltage range from −2 to 2 V under different conditions of ZnO doping and UV light illumination of a 350 nm wavelength. When no bending is applied to the sensors, Co-plus-Ni doping produced the highest photocurrent (I_{on}) of ~1.78 mA at 2 V, which is 5.6 times higher than that of CS (~0.32 mA), with a significant reduction in dark current (I_{off}) from 51 to 9 μA at 2 V, while separate Co and Ni dopings, respectively, exhibited I_{on} of 0.60 and 0.85 mA with I_{off} of 36 and 28 μA. This gives rise to a great increase in on–off current ratio (I_{on}/I_{off}) from 5.4 (CS) to 16.5 (Co-doped), 30.3 (Ni-doped), and 201.7 (Co + Ni-doped), as summarized in Figure 6. The significant increase in I_{on}/I_{off}, which is one of the important performance measures in photodiodes, is attributed to the improved crystalline quality of ZnO NRs by TM dopings, as revealed in our PL and XRD analysis. It was also shown by an earlier X-ray photoelectron spectroscopy (XPS) [7] that Co and/or Ni dopants tend to efficiently suppress the formation of non-stoichiometric defects, such as oxygen vacancies, carboxyl groups, or oxygenated hydrocarbons, through the effective binding of TM metals with oxygen due to their greater electronegativity than Zn.

The change in the electrical conductivity of ZnO NRs upon UV illumination is known to be associated with the chemisorption process of atmospheric O_2 on the ZnO surface, as described in Equations (2) and (3) [33].

$$(\text{Dark}) \ O_2 + e^- \rightarrow O_2^-{}_{adsorbed} \tag{2}$$

$$(\text{Under UV}) \ O_2^-{}_{adsorbed} + h^+ \overset{photon}{\rightarrow} O_2 \tag{3}$$

In dark conditions, atmospheric oxygen molecules trap the free electrons present on the surface of intrinsic n-type ZnO NRs and are adsorbed by the process shown in Equation (2). The electron concentration near the surface of NRs is therefore reduced, with the consequent expansion of the low-conductivity surface depletion layer, as illustrated in Figure 7a, and this gives rise to a very small current (I_{off}) through the NR–NR bridge between the IDE. Under UV illumination, the photo-generated holes recombine with electrons, leading to a desorption process of O_2 molecules, as shown in Equation (3), thereby decreasing the surface depletion width with the consequent increase in NR–NR bridge channel conductance (see Figure 7b), which produces an increased photocurrent (I_{on}). Trapping carriers in a dark state and detrapping them using the deep-level defects can give rise to higher I_{on} of the TM-doped devices, as explained by Al-Salman et al. [7,34]. Therefore, the density of deep-level defects can be significantly reduced by TM doping, and this suppresses the carrier recombination through the defect centers in ZnO crystals;

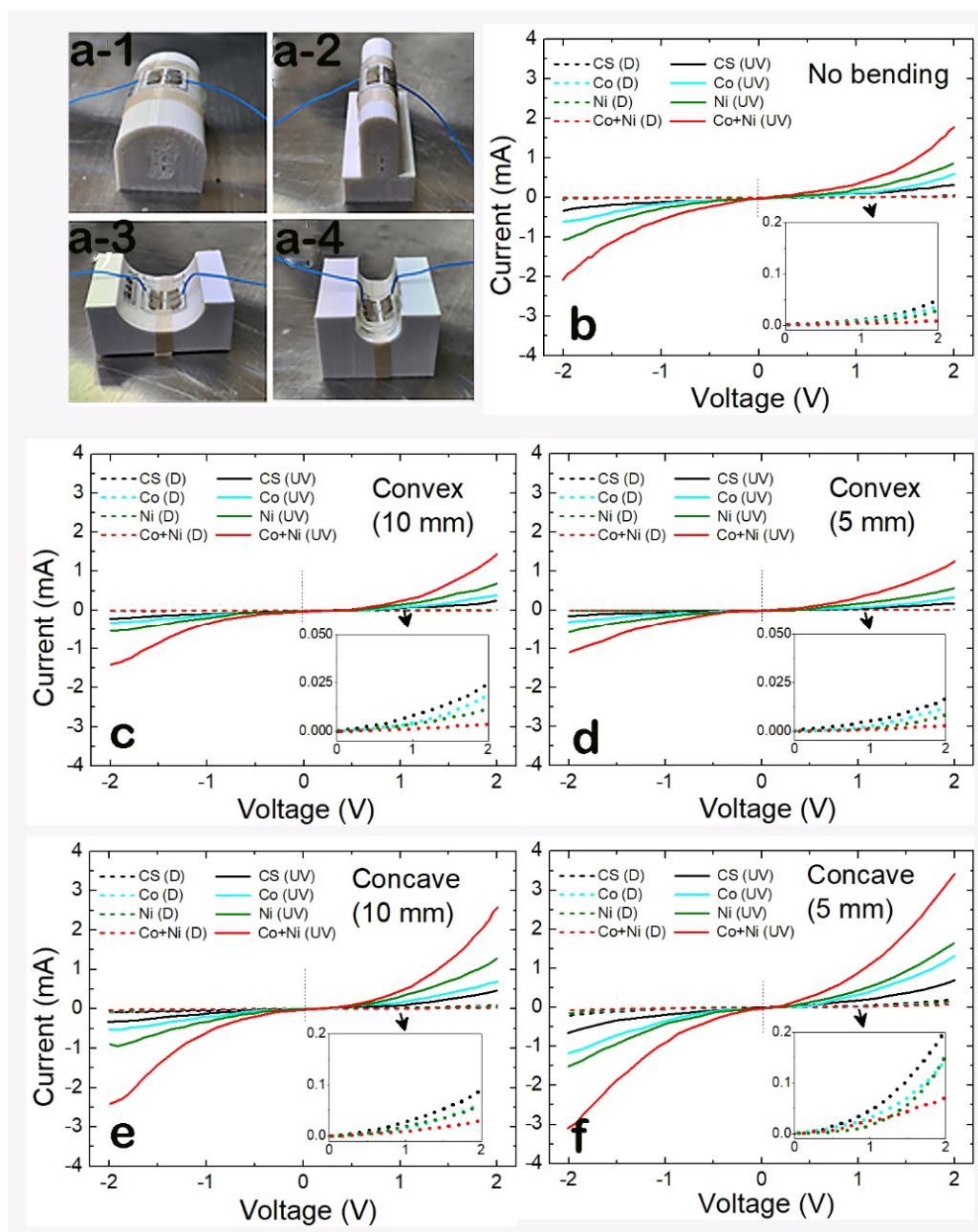thus, this eventually minimizes the loss of photo-generated carriers, producing an increase in I_{on}.

Figure 5. Sensor devices tested under two bending directions of (**a-1**,**a-2**) "convex" and (**a-3**,**a-4**) "concave". Micrographs of the devices measured in the ((**a-1**): 5 mm, (**a-2**): 10 mm) convex and ((**a-3**): 5 mm, (**a-4**): 10 mm) concave directions and under different bending radii (5 and 10 mm). I–V characteristics measured from the sensors prepared with different TM doping conditions (CS: undoped, Co: Co-doped, Ni: Ni-doped, Co + Ni: Co-plus-Ni-doped) according to their bending conditions of (**b**) no bending, convex bending with radii of (**c**) 10 (ε = 0.0175) and (**d**) 5 mm (ε = 0.0350), and concave bending with bending radii of (**e**) 10 and (**f**) 5 mm.
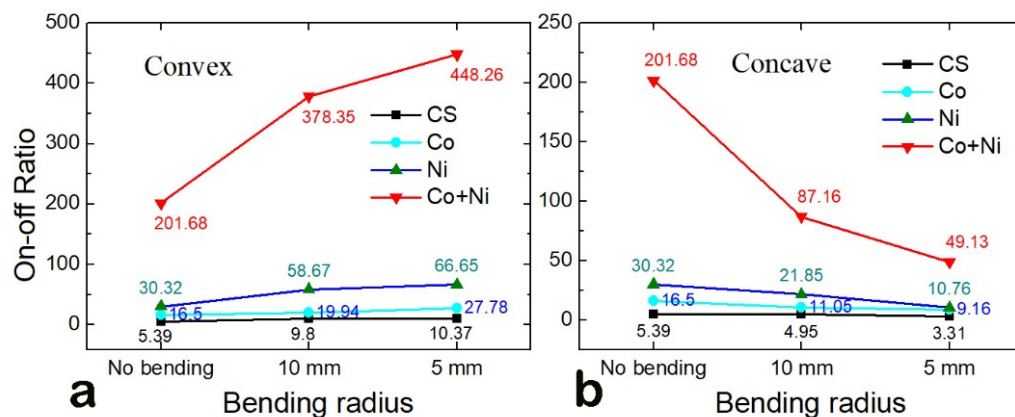
Figure 6. On/off current ratios measured from the sensor devices prepared under different TM doping conditions (CS: undoped, Co: Co-doped, Ni: Ni-doped, Co + Ni: Co-plus-Ni-doped). Photocurrent (on state) and dark current (off state) were measured at 2 V under (**a**) convex and (**b**) concave bending directions with bending radii of 10 and 5 mm ($\varepsilon = 0.0175$ and 0.0350).
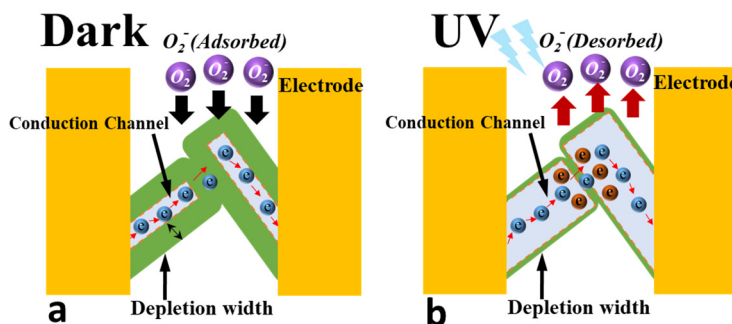

Figure 7. Schematics of the carrier transport through the cross-linking between ZnO NRs under (**a**) dark and (**b**) UV illumination conditions.

As shown in Figure 5, both I_{on} and I_{off} were also greatly affected by the bending direction and magnitude of the bending strain. Bending the device to the convex direction decreases both I_{on} and I_{off}; on the other hand, bending to the concave direction produces the opposite current change in I_{on} and I_{off}. One possible cause for this resistance change is the change in piezoresistance in ZnO crystals when subjected to either tensile or compressive state; however, this cannot reasonably describe the direction of changes in current as observed. Suppose the sensor is bent in the convex direction, as illustrated in Figure 8c, for example: all the nanowires must be under tensile stress state if they are cross-linked with solid physical contacts. This stress state needs to produce an increase in conductance, as observed from the earlier reports in piezotronic strain sensors [35], which, however, is the opposite to the current change we measured in this study. In the case of our device structure, the cross-linkings (see Figure 8) between the NRs carrying the current flow between the IDEs can be thought of as soft contacts; thus, it can be assumed that conductance changes upon bending, in our case, depend on the number of cross-links between the NRs. In the convex bending, we can expect a decrease in current measurement due to the effective reduction in the numbers of cross-linkings, as illustrated in Figure 8c, which provides good agreement with our I-V measurements, as shown in Figure 5.
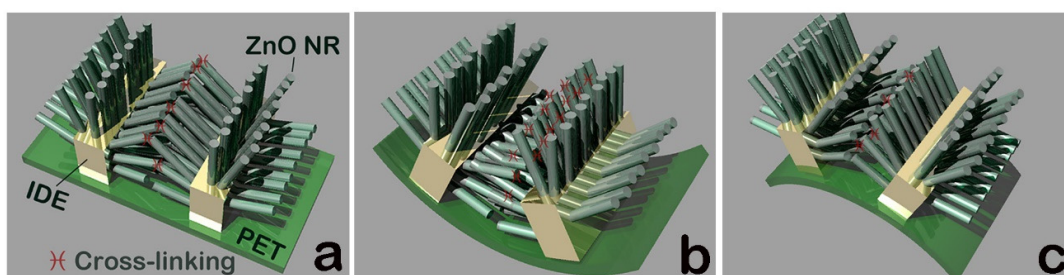
Figure 8. Schematic representation of the change in number of ZnO NR cross-linkings under the conditions of (**a**) no bending, (**b**) concave, and (**c**) convex bending.

Figure 6 shows the on–off current ratios of our sensor devices prepared by different TM dopings and measured under various bending directions and radii. As shown in the plots, I_{on}/I_{off} was increased with TM doping, and the highest ratio of ~448 was obtained from the case of Co-plus-Ni doping at a bending radius of 5 mm in the convex bending direction. On the other hand, the highest I_{on}/I_{off} of ~202 was measured under no bending condition in the concave bending direction. The on–off current ratio was increased with the increase in bending strain in the convex direction regardless of doping condition, but decreased in the concave direction, and this dependence of I_{on}/I_{off} on the bending strain is dominated by the greater change in the dark current compared to the photocurrent. For example, when bent at a radius of 5 mm to the convex direction and in the case of Co-plus-Ni doping, I_{off} is greatly reduced from ~17 to ~2.8 μA, whereas I_{on} is decreased from ~1.8 to ~1.2 mA at a much smaller rate, which gives rise to a consequent increase in I_{on}/I_{off} from ~202 to ~448. Nonetheless, the physics behind the relationship between bending strain and direction and the photoresponse characteristics was not fully understood; therefore, it is necessary to further examine how this can be associated with NR's microstructural properties, the change in cross-linkings upon bending strain/direction, and the energy barrier height change at the NR–NR junctions induced by the bending stress.

Real-time bending tests under different bending directions and radii were carried out at 1.5 V under normal room lighting. No bending strain was applied for the first 20 s; after that, a bending strain was applied to the sensor devices for 20 s. To examine whether the resistance was restored to the initial value, the devices were returned to no bending condition for the final 20 s. Figure 9 shows the normalized resistances in $\Delta R/R_0$ measured from the devices prepared under different TM doping conditions for the NRs, where ΔR and R_0 are the resistance change upon bending and the initial resistance of the no-bending state, respectively. In the case of convex bending, we obtained a positive ΔR from every device prepared under different NR doping conditions. This change in resistance is attributed to the reduction in the number of NR–NR cross-linkings, as was discussed earlier in Figure 6. On the other hand, negative ΔR values were measured when the concave bending was applied to the sensors, which is due to the increased numbers of cross-linkings.

To assess the sensing durability of our devices, 50 cyclic bending/release tests were performed with different bending directions and radii, as displayed in Figure 10. Stable sensing in our device structure depends on the reversible linkage and separation process at the NR–NR cross-linking points. All the devices, regardless of bending condition or ZnO doping condition, exhibited very stable resistances at peak (bending) and valley (release) points over the entire cycles. This indicates that the nature of cross-linkings between NRs is not cold-welding or permanent inter-material fusion at the surface between ZnO crystals but is most likely simple physical contact. To investigate the sensing performance, the gauge factors (GFs) of the sensors fabricated with NRs grown under different doping conditions were calculated and are summarized in Table 3. The GF is an important parameter demonstrating the sensitivity of resistive strain sensors, given by

$$GF = (\Delta R/R_0)/\varepsilon \tag{4}$$

where ε is the bending strain and $\Delta R/R_0$ is the normalized resistance change. As summarized in Table 3, the sensors showed that GF values ranged from 103 (CS, r = 10 mm) to 175 (Co + Ni doping, r = 10 mm) in the convex direction, while lower GF values from 46 (CS, r = 10 mm) to 83 (Co + Ni doping, r =10 mm) were extracted in the concave direction. As shown in Table 3, the sensor prepared with Co-plus-Ni-doped NRs showed the highest GF under all bending conditions. This corresponds to our material characterization results for the nanocrystals grown with Co-plus-Ni doping, where ZnO NRs of the best crystalline quality were shown in our XPS, PL, and XRD analyses. In the case of NR crystals of higher crystalline quality, the potential barrier height in the surface depletion area is relatively smaller. Therefore, even under very weak NR–NR bridge contact, a significant amount of current can be transported between the electrodes. On the other hand, in an NR–NR bridge with a larger surface potential barrier (lower crystalline quality), the current cannot be carried even through the same contact state. Due to this phenomenon, under the same bending strain, the Co-plus-Ni doping case can give rise to a larger $\Delta R/R_o$ as shown in Figure 9. In this case, a large number of NR–NR bridges in a weak contact state are likely to be disconnected at a faster rate during concave bending, while a greater number of NR–NR contact bridges can be formed during convex bending.
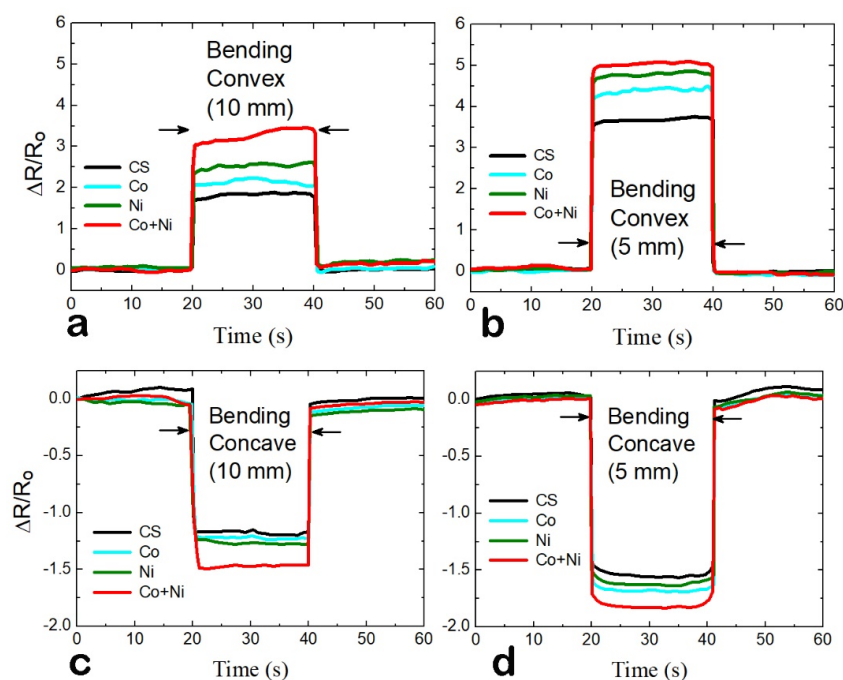

Figure 9. Transient characteristics of normalized resistance $\Delta R/R_0$ measured upon bending in the convex directions with radii of (**a**) 10 (ε = 0.0175) and (**b**) 5 mm (ε = 0.0350) and in the concave directions with bending radii of (**c**) 10 (**d**) 5 mm from the sensor devices prepared with different ZnO NR doping conditions.

Table 3. Bending strain GFs extracted from the IDE-based sensor devices fabricated with ZnO NRs of different TM dopings (CS, Co, Ni, Co + Ni) and characterized under various bending conditions (convex and concave bendings with two different bending radii of 5 and 10 mm).

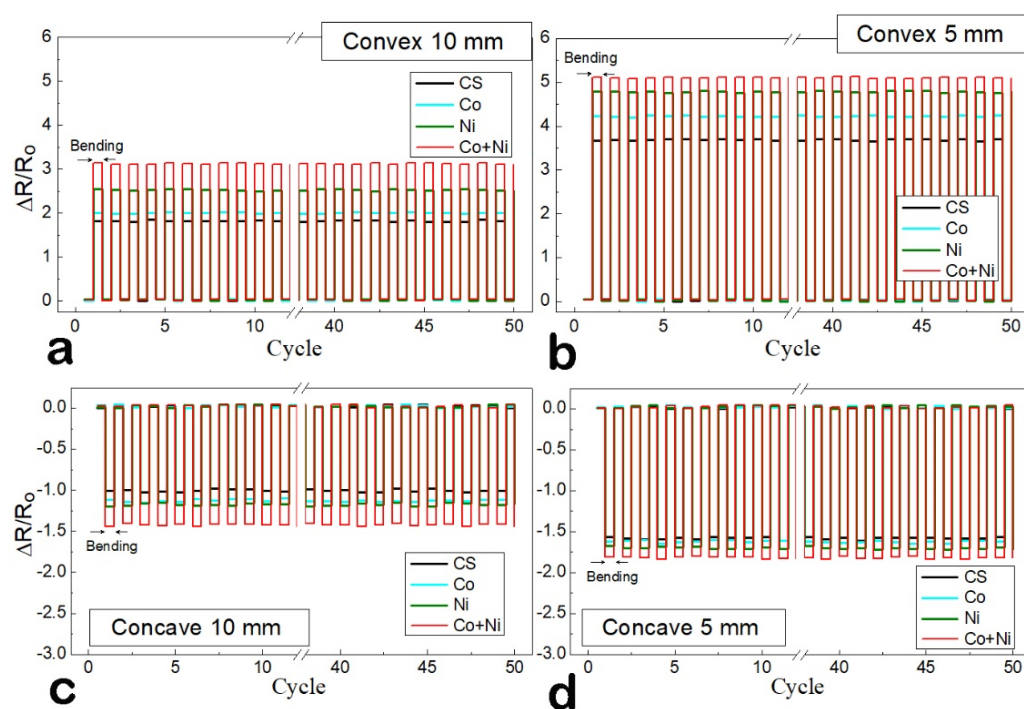| Bending Condition	GF			
	CS	**Co**	**Ni**	**Co + Ni**
Convex (10 mm, ε = 0.0175)	103	113	138	175
Convex (5 mm, ε = 0.0350)	105	120	136	145
Concave (10 mm, ε = 0.0175)	60	52	69	83
Concave (5 mm, ε = 0.0350)	46	45	49	52

Figure 10. Cyclic responses (50 cycles) of normalized resistance measured form the sensor devices prepared with different ZnO NR doping conditions (CS: undoped, Co: Co-doped, Ni: Ni-doped, Co + Ni: Co-plus-Ni-doped) and characterized upon bending in the convex direction with two different radii of (**a**) 10 (ε = 0.0175) and (**b**) 5 mm (ε = 0.0350) and in the concave direction with bending radii of (**c**) 10 (**d**) 5 mm.

In the case of axial strain sensors, a wide range of GFs was reported from the flexible sensors with ZnO piezoelectric fine wires (~1250) and vertical ZnO nanowire arrays (1000–1800), as well as the conventional semiconductor-based sensors such as Si-doped sensors (~200) and microsystems with suspended single-walled carbon nanotubes (600–1000) [35–38]. Various GFs were also reported from bending/torsion sensors using different nanostructures and piezoresistive materials, such as interlocking nanofibers (~11), gold nanowires (~7), and $Ti_3C_2T_x$ MXene thin films (~3.9) [39,40]. Table 4 shows a summary of important examples of nanostructure-based strain sensors and highly sensitive integrated flexible tactile sensors that have been reported to date. It needs to be noted that the GF values of 45–175 (ε = 1.75–3.5%) presented in this study are quite high compared to the bending/torsion sensors, considering that the higher reported GFs, such as in the cases of MXene thin films, were limited to much smaller strain range of 0–0.08%.

Table 4. Comparison of reported strain sensors.

Sensing Material [Ref.]	Strain Type/ Flexibility	Sensing Mechanism	Maximum GF	Strain Limit (%)
Single ZnO wire [35]	Axial/Flexible	Piezotronic	1250	1
Carbon nanotubes [36]	Axial/Rigid	Piezotronic	600–1000	0.6
Vertical ZnO nanowires [37]	Axial/Flexible	Piezotronic	1800	0.8
ZnO nanowires [38]	Axial/Flexible	Piezotronic	116	50
Gold nanowires [39]	Bending/Flexible	Resistive (contact)	1.8–7.4	25
$Ti_3C_2T_x$ MXene [40]	Bending/Flexible	Resistive (microcracks)	3.9	0.8
This work	Bending/Flexible	Resistive (cross-linking)	175	3.5

4. Conclusions

In summary, we demonstrated flexible bending sensors of high sensitivity and differential characteristics for bending direction, using a novel cross-linking structures between

ZnO NR arrays grown on IDEs patterns. We performed a comparative study to examine the performance of strain sensors fabricated with undoped NRs with those of TM-doped NRs. For this, various surface characterizations, such as PL, SEM, XPS, and XRD, were carried out to investigate the differences in the material properties of ZnO nanocrystals doped under different conditions that led to differences in sensing performance. ZnO NR crystals with TM dopings showed a significant improvement in their optical properties and (002) preferred growth orientation and, in the case of the photoresponse representing the crystalline quality of NR crystals, TM doping, especially in the case of Co-plus-Ni, showed the highest on–off current ratio. The sensor device prepared with NRs doped by Co-plus-Ni showed the best sensing performance, exhibiting the maximum GF of 175 at a bending strain of 1.75% in the convex direction. This TM sensor device depends on the low-temperature ZnO NR growth method with solution-based TM dopings; therefore, it can be extended to future applications for delicate and sensitive pressure, strain, and bending measurements in many stretchable systems, such as tissue/cell examination, smart skin design, electronic skin, medical prosthesis, and structural health monitoring. In addition, this multifunctional sensor, detecting high-sensitivity UV light and strain, can open a new path toward state-of-the-art sensors with facile low-temperature integration into future wearable electronics such as flexible touch-on displays, human–machine interfacing devices, and stretchable humanoid skins.

Author Contributions: Conceptualization, W.M.; investigation, W.M.; methodology, W.M.; formal analysis, W.M.; resources, S.-D.K.; data curation, W.M.; writing—original draft preparation, W.M.; writing—review and editing, W.M. and S.-D.K.; supervision, S.-D.K.; project administration, S.-D.K.; funding acquisition, S.-D.K. All authors have read and agreed to the published version of the manuscript.

Institutional Review Board Statement: Not applicable.

Informed Consent Statement: Not applicable.

Data Availability Statement: Not applicable.

Conflicts of Interest: The authors declare no conflict of interest.

References

1. Pantelopoulos, A.; Bourbakis, N.G. A Survey on Wearable Sensor-Based Systems for Health Monitoring and Prognosis. *IEEE Trans. Syst. Man Cybern. Part C* **2010**, *40*, 1–12.
2. Lou, Z.; Wang, L.; Jiang, K.; Wei, Z.; Shen, G. Reviews of Wearable Healthcare Systems: Materials, Devices and System Integration. *Mater. Sci. Eng. R Rep.* **2020**, *140*, 100523. [CrossRef]
3. Chiappim, W.; Fraga, M.A.; Furlan, H.; Ardiles, D.C.; Pessoa, R.S. The status and perspectives of nanostructured materials and fabrication processes for wearable piezoresistive sensors. *Microsyst. Technol.* **2022**, *28*, 1561–1580. [CrossRef]
4. Bhattacharya, S.; Srivastava, A. Synthesis and Characterization of Novel Cationic Lipid and Cholesterol-Coated Gold Nanoparticles and Their Interactions with Dipalmitoylphosphatidylcholine Membranes. *Langmuir* **2003**, *19*, 4439–4447. [CrossRef]
5. Hashim, A. Fabrication and characteristics of flexible, lightweight, and low-cost pressure sensors based on PVA/SiO$_2$/SiC nanostructures. *J. Mater. Sci. Mater. Electron.* **2021**, *32*, 2796–2804. [CrossRef]
6. Naganaboina, V.R.; Singh, S.G. Graphene-CeO$_2$ Based Flexible Gas Sensor: Monitoring of Low Ppm CO Gas with High Selectivity at Room Temperature. *Appl. Surf. Sci.* **2021**, *563*, 150272. [CrossRef]
7. Ajmal, H.M.S.; Khan, F.; Nam, K.; Kim, H.Y.; Kim, S.-D. Ultraviolet Photodetection Based on High-Performance Co-Plus-Ni Doped ZnO Nanorods Grown by Hydrothermal Method on Transparent Plastic Substrate. *Nanomaterials* **2020**, *10*, 1225. [CrossRef]
8. Xue, S.-S.; Tang, Z.-H.; Zhu, W.-B.; Li, Y.-Q.; Huang, P.; Fu, S.-Y. Stretchable and Ultrasensitive Strain Sensor from Carbon Nanotube-Based Composite with Significantly Enhanced Electrical and Sensing Properties by Tailoring Segregated Conductive Networks. *Compos. Commun.* **2022**, *29*, 100987. [CrossRef]
9. Cao, M.; Su, J.; Fan, S.; Qiu, H.; Su, D.; Li, L. Wearable Piezoresistive Pressure Sensors Based on 3D Graphene. *Chem. Eng. J.* **2021**, *406*, 126777. [CrossRef]

10. Hong, Y.J.; Saroj, R.K.; Park, W.I.; Yi, G.-C. One-Dimensional Semiconductor Nanostructures Grown on Two-Dimensional Nanomaterials for Flexible Device Applications. *APL Mater.* **2021**, *9*, 060907. [CrossRef]

11. Noh, Y.; Jeong, H.; Lee, D. Enhanced Ultraviolet Photodetector Using Zinc Oxide Nanowires with Intense Pulsed Light Post-Treatment. *J. Alloys Compd.* **2021**, *871*, 159537. [CrossRef]

12. Bagga, S.; Akhtar, J.; Mishra, S. Synthesis and applications of ZnO nanowire: A review. *AIP Conf. Proc.* **2018**, *1989*, 020004.

13. Bahramian, R.; Moshaii, A.; Eshghi, H. Effect of seeding modification of substrate on the growth and UV detection properties of ZnO nanowires. *Mater. Lett.* **2016**, *179*, 222–225.

14. Sharma, B.; Sharma, A.; Kim, J.-S. Recent advances on H_2 sensor technologies based on MOX and FET devices: A review. *Sens. Actuators B Chem.* **2018**, *262*, 758–770.

15. Neveling, D.P.; van den Heever, T.S.; Perold, W.J.; Dicks, L.M.T. A nanoforce ZnO nanowire-array biosensor for the detection and quantification of immunoglobulins. *Sens. Actuators B Chem.* **2014**, *203*, 102–110. [CrossRef]

16. Zhu, G.; Yang, R.; Wang, S.; Wang, Z.L. Flexible High-Output Nanogenerator Based on Lateral ZnO Nanowire Array. *Nano Lett.* **2010**, *10*, 3151–3155. [CrossRef]

17. Yu, Q.; Ge, R.; Wen, J.; Du, T.; Zhai, J.; Liu, S.; Wang, L.; Qin, Y. Highly sensitive strain sensors based on piezotronic tunneling junction. *Nat. Commun.* **2022**, *13*, 778. [CrossRef]

18. Hari, M.A.; Karumuthil, S.C.; Varghese, S.; Rajan, L. Performance Enhancement of Flexible and Self-Powered PVDF-ZnO Based Tactile Sensors. *IEEE Sens. J.* **2022**, *22*, 9336–9343. [CrossRef]

19. Supraja, P.; Sankar, P.R.; Kumar, R.R.; Prakash, K.; Jayarambabu, N.; Rao, T.V. Characteristics of 2D ZnO-Based Piezoelectric Nanogenerator and Its Application in Non-Destructive Material Discrimination. *Adv. Nat. Sci. Nanosci. Nanotechnol.* **2021**, *12*, 025011. [CrossRef]

20. Kang, B.-C.; Park, S.-J.; Ha, T.-J. Wearable Pressure/Touch Sensors Based on Hybrid Dielectric Composites of Zinc Oxide Nanowires/Poly(Dimethylsiloxane) and Flexible Electrodes of Immobilized Carbon Nanotube Random Networks. *ACS Appl. Mater. Interfaces* **2021**, *13*, 42014–42023. [CrossRef]

21. Habba, Y.; Capochichi-Gnambodoe, M.; Leprince-Wang, Y. Enhanced Photocatalytic Activity of Iron-Doped ZnO Nanowires for Water Purification. *Appl. Sci.* **2017**, *7*, 1185. [CrossRef]

22. Ajmal, H.M.S.; Khan, F.; Huda, N.U.; Lee, S.; Nam, K.; Kim, H.Y.; Eom, T.-H.; Kim, S.D. High-Performance Flexible Ultraviolet Photodetectors with Ni/Cu-Codoped ZnO Nanorods Grown on PET Substrates. *Nanomaterials* **2019**, *9*, 1067. [CrossRef]

23. Lee, S.; Nam, K.; Muhammad, W.; Shin, D.; Seo, S.; Kim, S.-D. Influence of N_2O plasma treatment on PET-based flexible bending sensors with ZnO nanorod array cross-linked with interdigitated electrode structures. *Ceram. Int.* **2022**, *48*, 25696–25704. [CrossRef]

24. Lim, J.H.; Lee, S.M.; Kim, H.-S.; Kim, H.Y.; Park, J.; Jung, S.-B.; Park, G.C.; Kim, J.; Joo, J. Synergistic effect of Indium and Gallium co-doping on growth behavior and physical properties of hydrothermally grown ZnO nanorods. *Sci. Rep.* **2017**, *7*, 41992.

25. Park, G.C.; Hwang, S.M.; Lim, J.H.; Joo, J. Growth behavior and electrical performance of Ga-doped ZnO nanorod/p-Si heterojunction diodes prepared using a hydrothermal method. *Nanoscale* **2014**, *6*, 1840–1847. [CrossRef]

26. Kegel, J.; Lar, F.; Povey, I.M.; Pemble, M.E. Defect-promoted photo-electrochemical performance enhancement of orange-luminescent ZnO nanorod-arrays. Phys. *Chem. Chem. Phys.* **2017**, *19*, 12255–12268. [CrossRef]

27. Khan, W.; Ajmal, H.M.S.; Khan, F.; Huda, N.U.; Kim, S.-D. Induced Photonic Response of ZnO Nanorods Grown on Oxygen Plasma-Treated Seed Crystallites. *Nanomaterials* **2018**, *8*, 371. [CrossRef]

28. Willander, M.; Nur, O.; Sadaf, J.R.; Qadir, M.I.; Zaman, S.; Zainelabdin, A.; Bano, N.; Hussain, I. Luminescence from Zinc Oxide Nanostructures and Polymers and their Hybrid Devices. *Materials* **2010**, *3*, 2643–2667. [CrossRef]

29. Liu, W.J.; Tang, X.; Tang, Z.; Bai, W.; Tang, N.Y. Oxygen Defects Mediated Magnetism of Ni Doped ZnO. *Adv. Condens. Matter Phys.* **2013**, *2013*, 424398. [CrossRef]

30. Djurišić, A.B.; Leung, Y.H.; Tam, K.H.; Ding, L.; Ge, W.K.; Chen, H.Y.; Gwo, S. Green, yellow, and orange defect emission from ZnO nanostructures: Influence of excitation wavelength. *Appl. Phys. Lett.* **2006**, *88*, 103107.

31. Kaur, N.; Sharma, S.K.; Kim, D.Y. Stress relaxation and transitions in optical bandgap of yttrium doped zinc oxide (YZO) thin films. *Curr. Appl. Phys.* **2016**, *16*, 231–239.

32. Kim, T.-W.; Lee, J.-S.; Kim, Y.-C.; Joo, Y.-C.; Kim, B.-J. Bending Strain and Bending Fatigue Lifetime of Flexible Metal Electrodes on Polymer Substrates. *Materials* **2019**, *12*, 2490. [CrossRef] [PubMed]

33. Ra, H.-W.; Khan, R.; Kim, J.T.; Kang, B.R.; Im, Y.H. The Effect of Grain Boundaries inside the Individual ZnO Nanowires in Gas Sensing. *Nanotechnology* **2010**, *21*, 085502. [CrossRef] [PubMed]

34. Al-Salman, H.S.; Abdullah, M.J. Fabrication and Characterization of Undoped and Cobalt-Doped ZnO Based UV Photodetector Prepared by RF-Sputtering. *J. Mater. Sci. Technol.* **2013**, *29*, 1139–1145. [CrossRef]

35. Zhou, J.; Gu, Y.; Fei, P.; Mai, W.; Gao, Y.; Yang, R.; Bao, G.; Wang, Z.L. Flexible piezotronic strain sensor. *Nano Lett.* **2008**, *8*, 3035–3040.

36. Cao, J.; Wang, Q.; Dai, H. Electromechanical Properties of Metallic, Quasimetallic, and Semiconducting Carbon Nanotubes under Stretching. *Phys. Rev. Lett.* **2003**, *90*, 15760.

37. Zhang, W.; Zhu, R.; Nguyen, V.; Yang, R. Highly sensitive and flexible strain sensors based on vertical zinc oxide nanowire arrays. *Sens. Actuators A* **2014**, *205*, 164–169.

38.   Xiao, X.; Yuan, L.; Zhong, J.; Ding, T.; Liu, Y.; Cai, Z.; Rong, Y.; Han, H.; Zhou, J.; Wang, Z.L. High-strain sensors based on ZnO nanowire/polystyrene hybridized flexible films. *Adv. Mater.* **2011**, *23*, 5440–5444.
39.   Gong, S.; Schwalb, W.; Wang, Y. A wearable and highly sensitive pressure sensor with ultrathin gold nanowires. *Nat. Commun.* **2014**, *5*, 3132.
40.   Bu, Y.; Shen, T.; Yang, W.; Yang, S.; Zhao, Y.; Liu, H.; Zheng, Y.; Liu, C.; Shen, C. Ultrasensitive Strain Sensor Based on Superhydrophobic Microcracked Conductive Ti_3C_2T MXene/Paper for Human-Motion Monitoring and E-Skin. *Sci. Bull.* **2021**, *66*, 1849–1857. [CrossRef]